

1 **Monsoon depression amplification by horizontal shear and humidity**
2 **gradients: a shallow water perspective**

3 D. L. Suhas^a and William R. Boos^{a,b}

4 ^a *Department of Earth and Planetary Science, University of California, Berkeley*

5 ^b *Climate and Ecosystem Sciences Division, Lawrence Berkeley National Laboratory*

7 ABSTRACT: Transient, synoptic-scale vortices produce a large fraction of total rainfall in most
8 monsoon regions and are often associated with extreme precipitation. However, the mechanism
9 of their amplification remains a topic of active research. For monsoon depressions, which are
10 the most prominent synoptic-scale vortex in the Asian-Australian monsoon, recent work has sug-
11 gested that meridional gradients in zonal wind in the vortex environment may produce growth
12 through barotropic instability, while meridional gradients in environmental humidity have also
13 been proposed to cause amplification through coupling with precipitating convection. Here, a
14 two-dimensional shallow water model on a sphere with parameterized precipitation is used to
15 examine the relative role played by these two environmental gradients. By systematically varying
16 the meridional moisture gradient and meridional wind shear for both weak, quasi-linear waves and
17 finite-amplitude isolated vortices, we show that rotational winds in the initial vortex are amplified
18 most strongly by meridional shear of the environmental zonal wind, while vortex precipitation
19 rates are most sensitive to environmental moisture gradients. The growth rate in the presence of
20 both gradients is less than the sum of growth rates in the presence of isolated gradients, as the
21 phase relation between moisture and vorticity anomalies becomes distorted with increasing shear.
22 These results suggest that background meridional gradients in both zonal wind and environmental
23 humidity can contribute to the amplification of vortices to monsoon depression strength, but with
24 some degree of decoupling of the dry rotational flow and the moist convection.

25 1. Introduction

26 Synoptic-scale low pressure systems are often observed in the vast South Asian and Australian
27 monsoon regions, as well as in the East Pacific where the intertropical convergence zone (ITCZ)
28 is positioned roughly 1,000 km north of the equator (Hurley and Boos 2015). These vortices
29 account for a large fraction of seasonal mean rainfall in monsoon regions (Godbole 1977; Hunt and
30 Fletcher 2019; Hurley and Boos 2015). In the Asian-Australian region, the more intense instances
31 of these systems are known as monsoon depressions, and are often associated with extreme rainfall
32 (Ajayamohan et al. 2010; Fletcher et al. 2018). Many attempts have been made to understand the
33 mechanisms governing the evolution of monsoon depressions and, more generally, monsoon low
34 pressure systems, invoking hydrodynamic instabilities that amplify the vortex at the expense of the
35 background winds (Mishra and Salvekar 1980; Saha and Chang 1983; Diaz and Boos 2019a,b) or
36 through its coupling with moist convection (Krishnamurti et al. 1976; Adames and Ming 2018a;
37 Diaz and Boos 2021a). However, the exact mechanism through which these weak disturbances
38 intensify into monsoon depressions remains a topic of active research (Clark et al. 2020; Diaz and
39 Boos 2021a,b).

40 A strong easterly vertical wind shear characterizes the region in which monsoon depressions form
41 leading many studies to invoke some form of baroclinic instability to explain the growth of monsoon
42 depressions (Mishra and Salvekar 1980; Saha and Chang 1983). These theories often require the
43 coupling of baroclinic instability with the condensation and precipitation of water (Moorthi and
44 Arakawa 1985; Salvekar et al. 1986; Krishnakumar et al. 1992). However, a key feature of all
45 forms of baroclinic instability is the upshear tilt of potential vorticity anomalies against the vertical
46 gradient in background zonal wind (Cohen and Boos 2016); this contrasts with the upright or slight
47 downshear tilt of potential vorticity in observed monsoon depressions (Keshavamurty 1972; Cohen
48 and Boos 2016). These results suggest that baroclinic instability is not the primary mechanism for
49 the growth of monsoon depressions.

50 Along with strong vertical wind shear, the South Asian monsoon also exhibits strong meridional
51 shear of the zonal wind (Figure 1b). A weaker but qualitatively similar wind shear is also observed
52 over the East Pacific (not shown), which is another region where synoptic-scale tropical vortices
53 grow. This meridional shear of zonal wind, hereafter referred to simply as horizontal shear, raises
54 the possibility that the monsoon basic-state may be barotropically unstable, with monsoon depres-

sions growing at the expense of the background horizontal shear. Early evidence for barotropic growth of monsoon depressions was mixed (Subrahmanyam et al. 1981; Nitta and Masuda 1981; Goswami et al. 1980; Lindzen et al. 1983; Shukla 1977; Krishnakumar et al. 1992; Rajamani and Sikdar 1989; Krishnamurti et al. 2013), although some studies arguing against barotropic instability as a relevant mechanism used basic-states that differed substantially from observations or focused on upper-tropospheric rather than lower-tropospheric modes; for a discussion see the last section of Diaz and Boos (2019a). Recent studies using three-dimensional basic-states drawn from modern reanalyses have shown that barotropic growth can explain the structure and propagation of observed monsoon depressions (Diaz and Boos 2019a,b). Barotropic conversion from the background meridional shear has also been shown to contribute to the energy of East Pacific easterly waves (Rydbeck and Maloney 2014). Nevertheless, even if barotropic growth is important, moist convection and diabatic heating likely play an essential role in achieving positive net growth rates in observed monsoon depressions, especially with frictional dissipation and a zonally asymmetric basic-state (Krishnamurti et al. 1976; Adames and Ming 2018a; Diaz and Boos 2021a).

An alternate route for the growth of monsoon depressions was proposed by Adames and Ming (2018a). Using a linear model, they showed the growth of a synoptic scale monsoon disturbance can occur due to interactions between meridional moisture advection, moist convection, and potential vorticity. This mechanism, termed moisture–vortex instability, favors growth in regions where the background specific humidity increases poleward, such as in South Asia (Figure 1a) and the East Pacific, and can operate even in the absence of barotropic or baroclinic instability. A similar instability was obtained by Sobel et al. (2001) in the limit of a weak temperature gradient balance. Adames (2021) further explored this mechanism in a linear two-layer quasi-geostrophic model, generalizing it to show that in the presence of a poleward MSE gradient (which might even exist due to a temperature gradient in the absence of moisture gradient), the instability grows at the expense of any baroclinic instability that may exist in monsoon regions. However, both Adames and Ming (2018a) and Adames (2021) used linear quasi-geostrophic models without background horizontal shear, which may not be relevant to observed monsoon depressions given their moderate Rossby numbers and the strongly sheared zonal winds in which they are embedded (Boos et al. 2015).

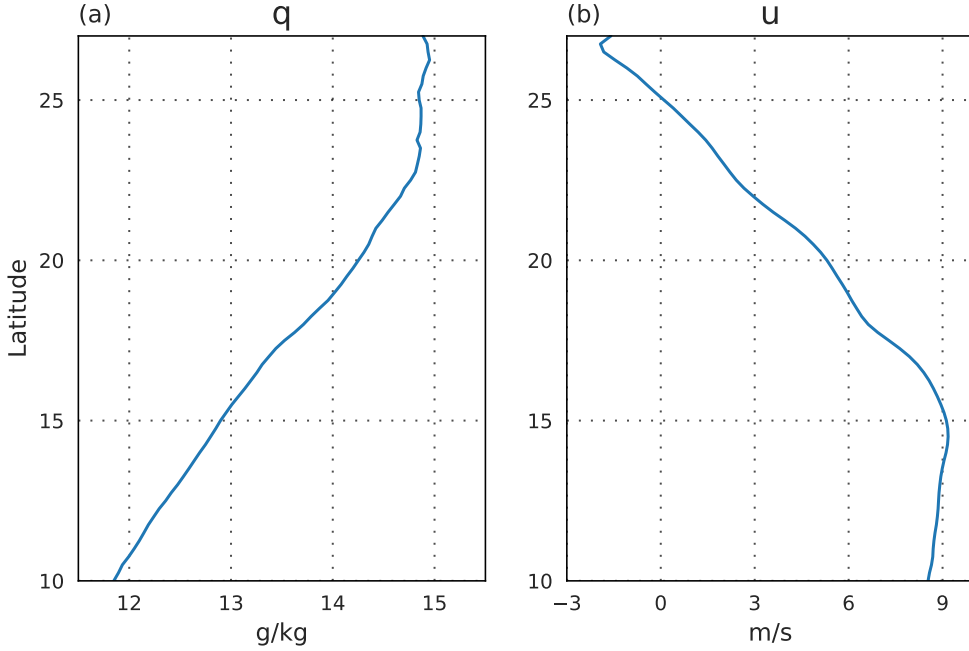


FIG. 1. The zonal mean of the JJAS basic-state (a) specific humidity and (b) zonal wind at 850 hPa over the South Asian region. The mean states are obtained by averaging the ERA5 data over the longitudes 80°E–90°E, and for the years 1979–2020. The plots are limited to 27°N, as the region northward of it is below the terrain surface. The region exhibits a moisture gradient which increases with latitude and a meridional wind shear, centred roughly around 20°N.

Here we use a fully non-linear model to examine the evolution of disturbances in a basic-state with both strong meridional moisture gradients and strong zonal flow. Specifically, we examine the growth of monsoon depression-like vortices using a two-dimensional shallow water model with parameterized moist convection. As recent studies have suggested that baroclinic instability is inconsistent with the growth of observed monsoon depressions (Cohen and Boos 2016), we mainly consider the roles played by barotropic instability and moisture–vortex instability. This work is complementary to the simulations conducted with more complex cloud-system resolving models (Diaz and Boos 2019b) and global climate models (Adames and Ming 2018b), because it enables us to more cleanly control the separate and combined influences of gradients in humidity and wind. The model used here also allows us to simulate the non-linear evolution of finite-amplitude vortices without linearization and the quasi-geostrophic approximation.

100 We aim to determine how barotropic instability and moisture–vortex instability might interact
 101 when a monsoon depression-like vortex exists in a basic-state with meridional gradients in both
 102 humidity and zonal wind. Are both gradients needed for growth, or is moist convection without
 103 a moisture gradient sufficient? Do the two instability mechanisms amplify or inhibit each other?
 104 The model framework and numerical details are discussed in the next section. The growth of weak,
 105 quasi-linear sinusoidal vorticity anomalies are examined in Section 3, then the evolution of strong
 106 isolated vortices is presented in Section 4. Section 5 interpret some of these results and conclusions
 107 are summarized in Section 6.

108 2. Model details

109 This study uses a single-layer moist shallow water model on a rotating sphere, of the form (Gill
 110 1982; Bouchut et al. 2009; Zeitlin 2018; Suhas and Sukhatme 2020)

$$\begin{aligned}
 \frac{\partial \zeta}{\partial t} + \nabla \cdot (\mathbf{u} \zeta_a) &= 0, \\
 \frac{\partial \delta}{\partial t} - \mathbf{k} \cdot \nabla \times (\mathbf{u} \zeta_a) &= -\nabla^2 \left(\frac{\mathbf{u} \cdot \mathbf{u}}{2} + gh \right), \\
 \frac{\partial h}{\partial t} + \nabla \cdot (\mathbf{u} h) &= -\chi \mathcal{P}, \\
 \frac{\partial q}{\partial t} + \nabla \cdot (\mathbf{u} q) &= -\mathcal{P}.
 \end{aligned} \tag{1}$$

111 The above system contains the vorticity equation, the divergence equation, the mass continuity
 112 equation, and a moisture equation, in that sequence. In these equations, $\mathbf{u} = (u, v)$ is the horizontal
 113 flow, ζ is the relative vorticity, ζ_a is the absolute vorticity and δ is the divergence. The shallow
 114 water layer has a depth of $h(x, y, t)$, with H being the undisturbed mean of $h(x, y, t)$ (the value of
 115 which is discussed below).

116 The moisture equation governs the evolution of the column water vapor (q), with precipitation
 117 (\mathcal{P}) acting as a moisture sink. Precipitation is modeled using a Betts-Miller form (Betts 1986)
 118 dependent on the column water vapor (Muller et al. 2009), specifically $\mathcal{P} = (q - q_s) \Theta(q - q_s) / \tau_c$,
 119 where q_s is the prescribed saturation column water vapor, $\tau_c = 12$ h is the condensation timescale
 120 and Θ is the Heaviside function (Suhas and Sukhatme 2020). Moisture couples to the mass equation
 121 through precipitation, with χ acting as a conversion factor similar to the latent heat. Since we are

122 mainly interested in the growth of anomalies over the initial few days of model time, no large scale
123 forcing, damping, or surface evaporation is included.

124 This model formulation has been used to study the development of fronts and non-linear waves
125 (Bouchut et al. 2009), the emergence of modons and geostrophic adjustment (Rostami and Zeitlin
126 2019a,b), the transient, precipitating response to tropical forcings and the influence of moisture
127 gradients (Suhas and Sukhatme 2020), and the effects of moisture on barotropic and baroclinic
128 instability (Lambaerts et al. 2011, 2012; Rostami and Zeitlin 2017; Bembenek et al. 2021). While
129 some studies have shown that barotropic instability can intensify in the presence of water con-
130 densation (Lambaerts et al. 2011; Rostami and Zeitlin 2017), those studies did not examine the
131 influence of a horizontal moisture gradient nor consider a monsoon-like basic-state. Here, our aim
132 is to examine the growth of the vortex in the presence of a moisture gradient without resorting to
133 these restrictions.

134 The shallow water equations are solved using a pseudo-spectral method on a sphere using a
135 library for spherical harmonic transforms for numerical simulations (SHTns; Schaeffer 2013). The
136 simulations are run at a resolution of 512 (longitude) \times 256 (latitude), and triangularly truncated
137 with a maximum resolved wavenumber of 170 . Time stepping uses a third-order Adams-Bashforth
138 integrator with a time step of 30 s and a Δ^4 hyperviscosity for small scale dissipation.

139 A wide range of mean heights H have been used by various studies, with values ranging from a
140 few hundred metres to a few kilometres. While a mean height of $200 - 300$ m corresponds to the
141 dry phase speeds of the first baroclinic mode in the tropics (Wheeler et al. 2000; Kraucunas and
142 Hartmann 2007), larger heights are necessary to generate the observed mean states of the zonal
143 flows in the mid-latitudes (Galewsky et al. 2004; Paldor et al. 2021). Our results are not greatly
144 affected by this choice of H (we looked at values of H ranging from 300 m to 10 km), but to
145 accommodate the strong meridional height gradients necessary to generate the required basic-state
146 zonal flow, we chose a basic-state depth of 1000 m; this yields a dry Kelvin wave speed (c_d) of
147 about 100 m s^{-1} (Kraucunas and Hartmann 2007; Monteiro et al. 2014).

148 The choice of moist parameters q_s and χ is somewhat arbitrary, as only the product χq influences
149 the coupling of moisture with the dynamics. We set the maximum magnitude of q_s to 1 m, and
150 select $\chi = 900$. This yields a moist Kelvin wave speed, $c_m \approx 0.3c_d$ (Bouchut et al. 2009; Frierson
151 et al. 2004). The model is initialized with a state of saturation (i.e., $q = q_s$), so at initial times the

152 gradient of prescribed saturation column water vapor sets the gradient of the moisture field. We
 153 introduce a delay in the convective onset by setting the value of the condensation time scale $\tau_c =$
 154 12 h, which has been used in other theoretical models of the Asian monsoon (Adames and Ming
 155 2018a).

156 We use two types of initial perturbations. First, we study the response to small-amplitude
 157 sinusoidal vorticity anomalies, which allows us to examine the evolution of a disturbance of
 158 a single wavenumber without strong non-linear effects. Next, we consider a more non-linear
 159 scenario, where the initial perturbation takes the form of a finite-amplitude, isolated vortex. Both
 160 of these types of initial perturbations are centred at 20°N , a typical latitude at which many monsoon
 161 depressions form (Sikka 1978); our conclusions are insensitive to small variations in the choice
 162 of base latitude. We explore the time evolution of these initial perturbations in the presence
 163 of a varying meridional basic-state moisture gradient, q_{sy} , and a varying meridional wind shear
 164 expressed as a localized basic-state vorticity maximum, ζ_s ; sample basic-state moisture and wind
 165 profiles are shown in Figure 2. The strength of the horizontal wind shear is controlled by varying
 166 the magnitude of an imposed vorticity strip, following Diaz and Boos (2021a). For simplicity, we
 167 have centred both the basic-state moisture gradient and horizontal shear zone near 20°N , although
 168 in the observed South Asian mean state they are centred slightly away from this latitude (Figure 1).

175 3. Quasi-linear sinusoidal modes

176 We examine the response of our shallow water system to small amplitude sinusoidal vorticity
 177 anomalies for a range of basic-state moisture gradients (q_{sy}) and horizontal wind shears (ζ_s). This
 178 choice of a weak initial perturbation ensures that the growth is nearly linear, at least in the initial
 179 stages. The sinusoidal vorticity anomaly is centred at $\phi_0 = 20^\circ\text{N}$ and is of the form

$$\zeta'(\lambda, \phi) = \zeta_{pert} \sin(k\lambda) \exp \left[- \left(\frac{\phi - \phi_0}{\Delta\phi} \right)^2 \right]$$

180 where the perturbation magnitude $\zeta_{pert} = 1 \times 10^{-7} \text{ s}^{-1}$, $k = 15$ is the zonal wavenumber, λ is longi-
 181 tude, ϕ is latitude, and $\Delta\phi = 5^\circ$. We also performed experiments with varying zonal wavenumbers
 182 and, similar to Adames and Ming (2018a), found that in the presence of a basic-state moisture
 183 gradient, the eddy energy growth was strongest around wavenumber $k = 15$. With basic-state

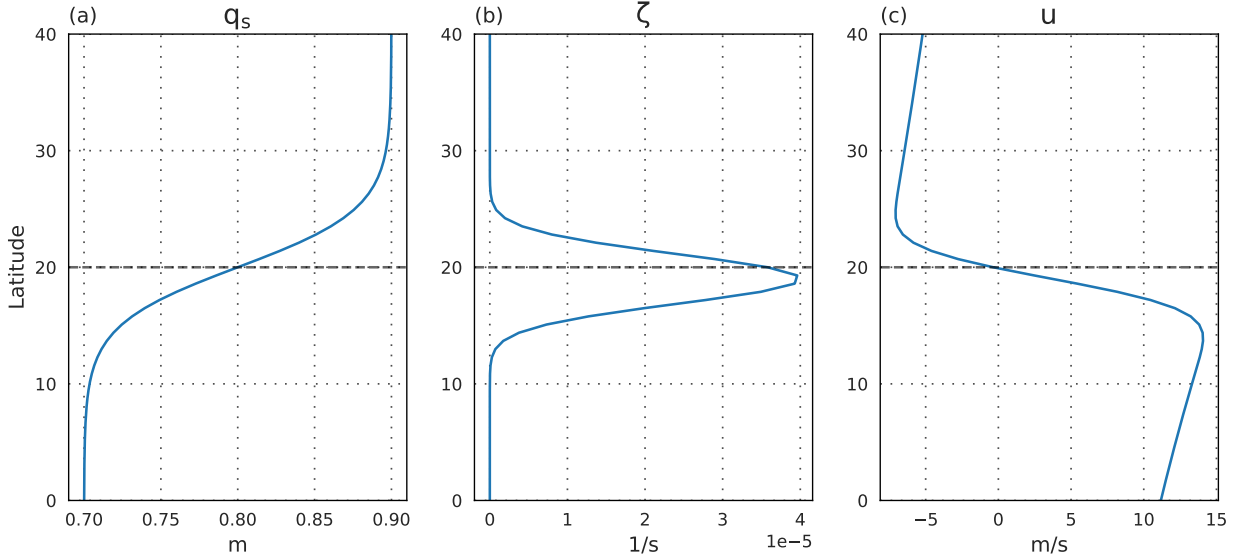


FIG. 2. Profile of the (a) imposed saturation column water vapor (q_s) and (b) gaussian vorticity strip which yields a (c) meridionally sheared zonal wind. Here, the basic-state saturation moisture has a gradient of $q_{sy} = 0.2$ m, and the wind shear is $\zeta_s = 4 \times 10^{-5} \text{ s}^{-1}$. All the saturation moisture profiles considered in this study have a value of 0.8 m at 20°N , and the gradient value refers to the maximum change in magnitude between the equator and the pole. Zonal wind has a zero-crossing at 20°N . For convenience, we refer the wind shear with the magnitude of the corresponding vorticity strip.

horizontal wind shear and no moisture gradient, the fastest growth was also found in the vicinity of $k = 15$. Hence, we only present results for initial anomalies with zonal wavenumber 15.

To begin, we study the evolution of an initial sinusoidal anomaly without basic-state shear or moisture gradients, in order to confirm that at least one of these basic-state properties is needed for anomaly growth. In this set of experiments, basic-state horizontal wind shear is absent ($\zeta_s = 0$). The moist coupling parameter (χ) is set to 0 in a dry configuration, while in a moist run we impose a uniform background moist saturation field ($q_{sy} = 0$, i.e., no basic-state moisture gradient). The main objective here is to see whether an anomaly can grow in the absence of both basic-state gradients, and how the inclusion of moisture modifies the dry solution. Results from these experiments can also serve as a reference for comparison with solutions obtained with basic-state gradients. For both the dry and moist (uniform basic-state moisture) runs, the initial eddy energy, which includes both eddy potential and kinetic energy, decays at a rate of -0.02 day^{-1} and there are no significant differences between the dry and moist runs. In the absence of large scale damping, hyperviscosity

is responsible for this decay. Other dynamical variables, as well as precipitation in the moist run, show a similar decay with time. This indicates that interaction of a weak initial vortex with the release of latent heat alone is insufficient for growth, consistent with the cloud-system-resolving simulations of tropical depression spinup conducted by Murthy and Boos (2018).

a. Solutions with a basic-state moisture gradient

We now introduce a northward-increasing basic-state moisture field, systematically varying the gradient of the saturation profile (q_{sy}) and studying the influence of this basic-state property on the amplification of our initial weak, sinusoidal vorticity anomalies. We eliminate possible barotropic growth by setting the basic-state horizontal wind shear (ζ_s) to 0. The prescribed basic-state saturation column water vapor is of the form

$$q_s(\phi) = q_{s0} + \frac{q_{sy}}{2} \tanh\left(\frac{\phi - \phi_0}{\Delta\phi}\right)$$

where $\phi_0 = 20^\circ$ and $\Delta\phi = 5^\circ$. Here, q_{s0} sets the value of the basic-state q_s at 20°N and q_{sy} controls the meridional gradient of the background moist saturation field. A typical profile with $q_{s0} = 0.8$ m and a gradient of $q_{sy} = 0.2$ m (maximum change from equator to pole) is shown in Figure 2a. This gradient value of 0.2 m is qualitatively similar to the fractional change in the observed water vapor mixing ratio (Diaz and Boos 2019b) and precipitable water (Chen et al. 2018) over South Asia, which varies meridionally by about 20% – 30% (Figure 1a). Further, for ease of comparison, all experiments use the same moist saturation value of $q_s = 0.8$ m at 20°N , with the basic-state moisture gradient (q_{sy}) varying from 0 (uniform moist case) to 0.4 m (with that maximum gradient setting q_s to 1 m on the poleward side of the gradient zone).

For the basic-state with no moisture gradient, $q_{sy} = 0$, precipitation occurs to the east of the cyclonic vortex centre (Figure 3a). This is in contrast to the observations, where peak precipitation occurs to the west-southwest of the vortex centre (Godbole 1977). In contrast, with a basic-state moisture gradient $q_{sy} = 0.2$ m, precipitation occurs to the west of the cyclonic vortex centre and anomalies strengthen with time and propagate westward (Figure 4). Eddy energy has a growth rate of 0.17 day^{-1} , close to the value of 0.23 day^{-1} obtained in the linear β -plane model used by Adames and Ming (2018a), which also imposed a meridional temperature gradient. As diabatic heating enhances positive vorticity anomalies, cyclones grow faster than anticyclones (Figure 4).

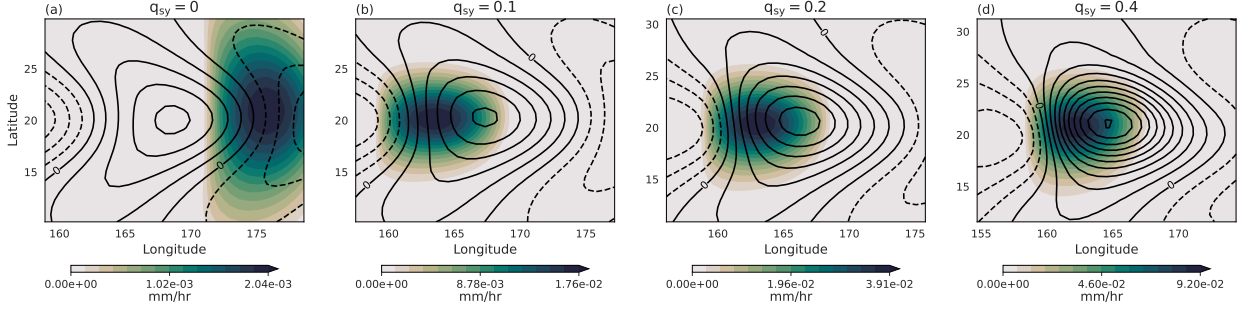


FIG. 3. Precipitation rate (color) and vorticity (black, with a contour interval of $2 \times 10^{-8} \text{ s}^{-1}$) at day 3 for the experiments with varying basic-state moisture gradients (q_{sy}) and no wind shear ($\zeta_s = 0$). These are the response to small amplitude sinusoidal vorticity anomalies. The plot is centred at the maxima of one of the vortices. Precipitation occurs to the west of the vortex centre except for the case with a zero moisture gradient, where it occurs to the east of the vortex centre and is significantly weaker.

The growth rates of vorticity, horizontal wind, and precipitation all increase with the basic-state moisture gradient (Figures 3 and 5). The uniform saturation case ($q_{sy} = 0$) provides a useful contrast, as its precipitation occurs to the east of cyclonic vortices and its vorticity and precipitation decays with time, supporting the idea that a spatial structure in which peak precipitation lies west of peak vorticity is necessary for growth. The dynamical fields as well as the precipitation rate strengthens with increasing basic-state moisture gradient. The absolute precipitation rates in these simulations are not especially meaningful given the weak, quasi-linear nature of the disturbances and the fact that it is the product χP that couples with the dynamics. The sharp changes seen in the maximum meridional velocity around day 4 (Figure 5a) is due to the maxima operator selecting different parts of the vortex, as time evolves.

We also assessed the sensitivity of our solutions to the zonal wavenumber and convective time scale. Broadly, our results agree with the solutions obtained by Adames and Ming (2018a), with strongest growth found around zonal wavenumber $k = 15$ and a convective time scale $\tau_c = 12 \text{ h}$. As in Adames and Ming (2018a), we also find the precipitation shifts away from the vortex centre with decreasing τ_c .

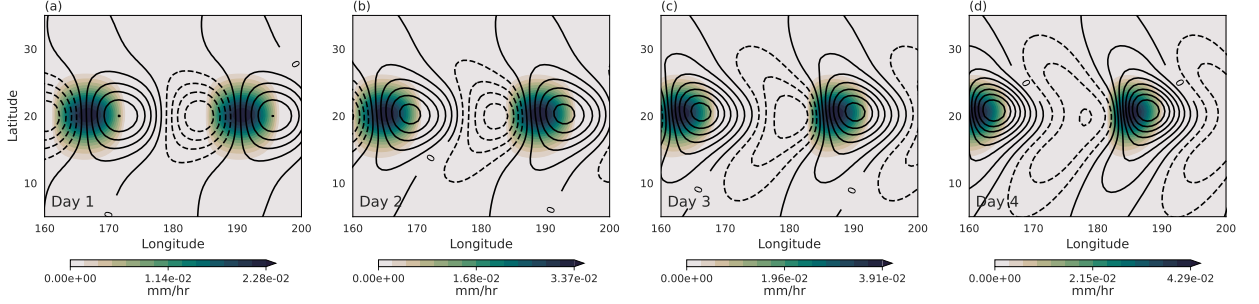


FIG. 4. The evolution of precipitation rate (color) and vorticity (black, with a contour interval of $2 \times 10^{-8} \text{ s}^{-1}$) with time for the experiment with a basic-state moisture gradient $q_{sy} = 0.2 \text{ m}$ and no wind shear ($\zeta_s = 0$). The system is initially perturbed by small amplitude sinusoidal vorticity anomalies centred at 20°N . The initial disturbance is strengthening with time and is propagating to the west.

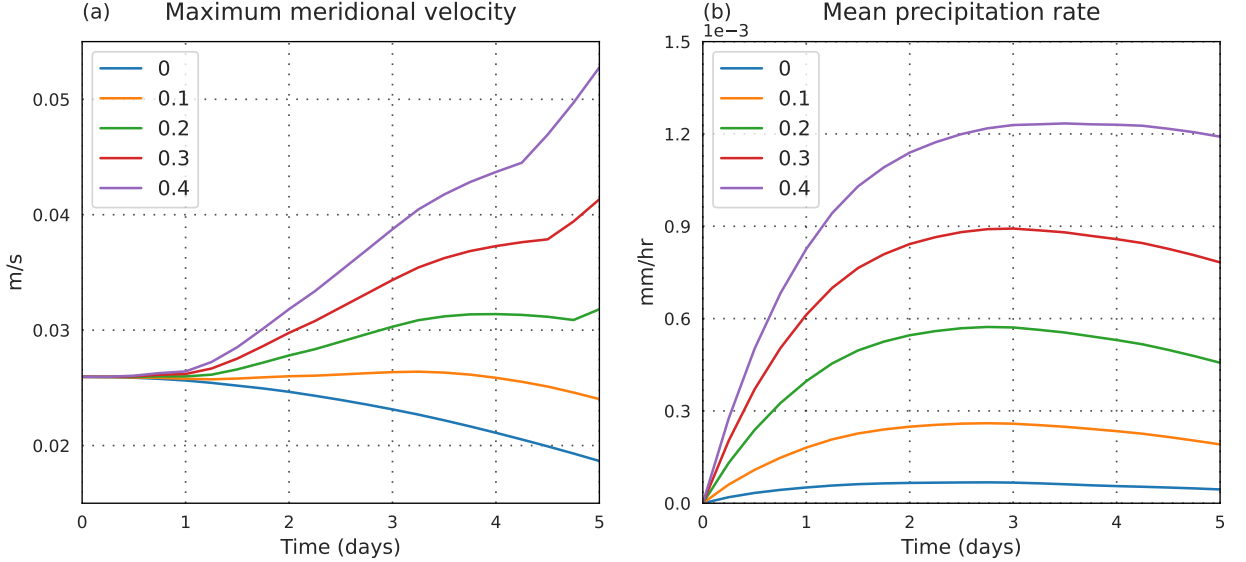


FIG. 5. Time series of the (a) maximum meridional velocity and (b) mean precipitation rate for the experiments with varying basic-state moisture gradients (q_{sy}) and no wind shear ($\zeta_s = 0$). These values are averaged over the entire domain and are the response to small amplitude sinusoidal vorticity anomalies.

b. Solutions with basic-state horizontal shear

We now examine the evolution of the weak, sinusoidal vorticity anomalies in the presence of horizontal wind shear and a uniform moisture background ($q_{sy} = 0$). Based on the observed mean state of the South Asian monsoon (Figure 1a), we construct a background wind shear using a

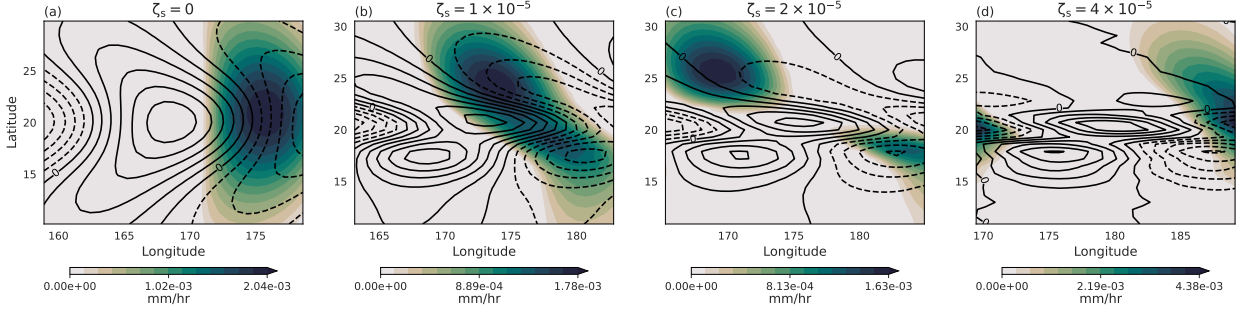


FIG. 6. Precipitation rate (color) and vorticity (black, with a contour interval of $5 \times 10^{-8} \text{ s}^{-1}$) at day 3 for the experiments with varying wind shear (ζ_s) but with no basic-state moisture gradient ($q_{sy} = 0$). The system is initially perturbed by small amplitude sinusoidal vorticity anomalies centred at 20°N . The vorticity contours are plotted after removing the imposed background shear. The domain is centred at the maxima of one of the vortices.

vorticity strip,

$$\zeta(\phi) = \zeta_s \exp \left[- \left(\frac{\phi - \phi_0}{\Delta\phi} \right)^2 \right]$$

where $\phi_0 = 19^\circ$ and $\Delta\phi = 3^\circ$. The parameter ζ_s controls the magnitude of the basic-state shear and yields a zonal wind profile with a zero-crossing at 20°N (Diaz and Boos 2019a, 2021a). Typical profiles of vorticity and the corresponding zonal wind for $\zeta_s = 4 \times 10^{-5} \text{ s}^{-1}$ are shown in Figure 2b, c.

Vorticity and precipitation at day 3 for various magnitudes of shear (ζ_s) are shown in Figure 6. As we saw earlier, in the absence of a meridional moisture gradient, precipitation occurs east of cyclonic vortex centres and is an order-of-magnitude weaker than in the basic-state having a moisture gradient but no shear (compare magnitudes of precipitation between Figures 5b and 7b). In the absence of a basic-state moisture gradient, precipitation is driven by convergence (which in this model serves as a proxy for the generation of convective instability by ascent) rather than the horizontal advection of moisture, which explains the weaker magnitude of precipitation and its position to the east of the cyclonic vortex in the region of convergence (see Figure 3 in Kiladis et al. (2009) for similar structures in theoretical equatorial waves). In contrast, horizontal wind anomalies are stronger for the basic-state with shear than for the basic-state with only a moisture

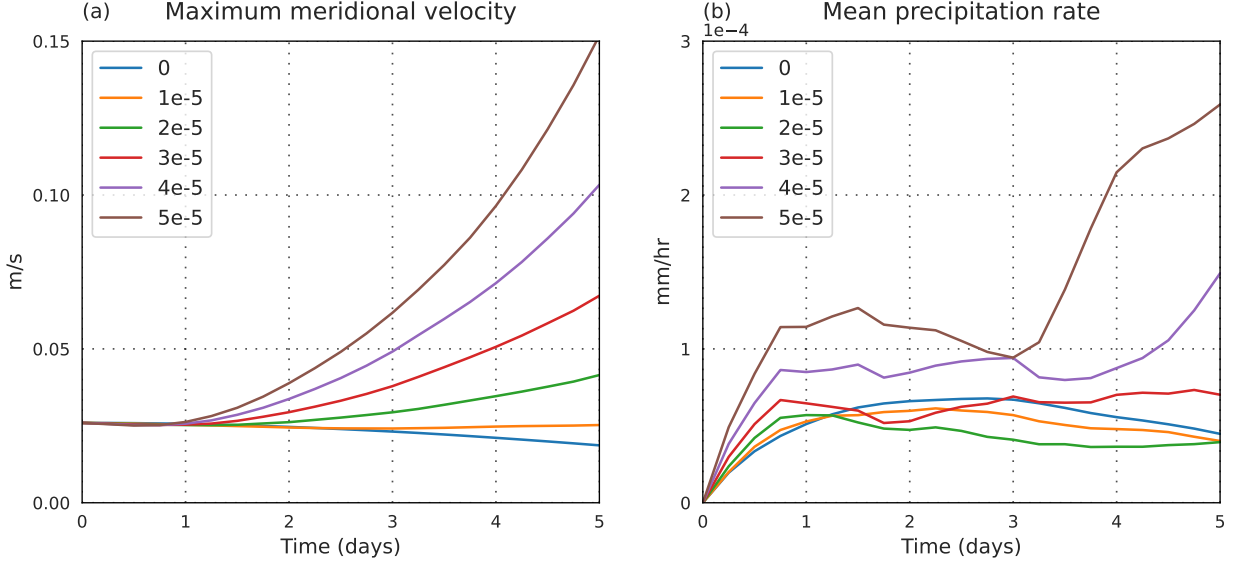


FIG. 7. Time series of the (a) maximum meridional velocity and (b) mean precipitation rate for the experiments with varying horizontal wind shear (ζ_s) but with no basic-state moisture gradient ($q_{sy} = 0$). These values are averaged over the entire domain and are the response to small amplitude sinusoidal vorticity anomalies.

gradient. With increasing shear, the initial sinusoidal fields become progressively distorted and precipitation becomes spatially decoupled from the vortex centre. The circulation anomalies, as indicated by the meridional wind, grow stronger with shear, but the precipitation rate displays less sensitivity (Figure 7; although precipitation increases greatly after day 3 for strong horizontal shears, this occurs far from the cyclonic vorticity centres and thus does not resemble the behavior of observed monsoon low pressure systems). The up-shear tilt of the perturbations and the absence of any other instability mechanisms suggest that the growth of the vorticity anomalies is due to barotropic instability (Peng et al. 2009). In essence, barotropic instability amplifies the circulation anomalies, but the growth rate of precipitation has less sensitivity to the shear in the absence of a moisture gradient.

c. Solutions with a basic-state moisture gradient and horizontal shear

We now examine solutions for basic-states with both moisture gradients and horizontal shear, showing that the decoupling of precipitation from circulation anomalies, suggested in the experiments described above, becomes even more evident when these basic-state gradients are combined.

292 The time evolution of the maximum meridional velocity and mean precipitation rate for various
 293 moisture gradients with fixed horizontal shear is shown in Figures 8a and 8b. While the meridional
 294 velocity increases with time (Figure 8a), there is little sensitivity in the growth rate of meridional
 295 velocity to changes in the moisture gradient. The maximum meridional velocities achieved with
 296 this intermediate basic-state shear are roughly twice as large as those achieved with the strongest
 297 moisture gradient in the absence of horizontal shear (compare with Figure 5a), but the peak merid-
 298 ional velocities actually decrease slightly as the basic-state moisture gradient is increased. This
 299 suggests that the circulation anomalies are mostly driven by barotropic instability, and indeed their
 300 growth rate increases strongly with the basic-state shear (Figure 8c). In contrast, precipitation is
 301 strongly affected by the moisture gradient (Figure 8b), exhibiting little sensitivity to horizontal
 302 shear with a fixed moisture gradient (Figures 8d; as in Figure 7b, the increase in precipitation
 303 after day 3 occurs far from the cyclonic vorticity centre and thus is a poor analogue for observed
 304 monsoon depressions at that stage of the instability).

309 A summary of all the runs is presented in Figures 9a-c, which show the amplification of the
 310 maximum meridional velocity and mean precipitation rate at day 3, relative to the moist run with
 311 no basic-state moisture gradient and no horizontal shear ($q_{sy} = 0$, $\zeta_s = 0$), together with the eddy
 312 energy growth rates averaged over days 2 – 4. The maximum meridional velocity and eddy energy
 313 growth depend strongly on the horizontal shear but only weakly on the moisture gradient, with an
 314 increase in the moisture gradient causing a modest increase in these dynamical measures for weak
 315 shear and a slight decrease for strong shear. In contrast, the mean precipitation rate is determined
 316 primarily by the moisture gradient.

324 **4. Nonlinear isolated vortices**

325 Now we consider a more realistic case, using the same basic-states but where the initial pertur-
 326 bation takes the form of an isolated vortex strong enough to produce nonlinear effects. This vortex
 327 is intended to represent an idealized weak low pressure system that might intensify into a monsoon
 328 depression, and we examine how it evolves in basic-states with different moisture gradients and
 329 horizontal wind shear. The initial vortex is generated using a height anomaly,

$$h'(\lambda, \phi) = h_{pert} \exp \left[- \left(\frac{\lambda - \lambda_0}{\Delta \lambda} \right)^2 \right] \exp \left[- \left(\frac{\phi - \phi_0}{\Delta \phi} \right)^2 \right]$$

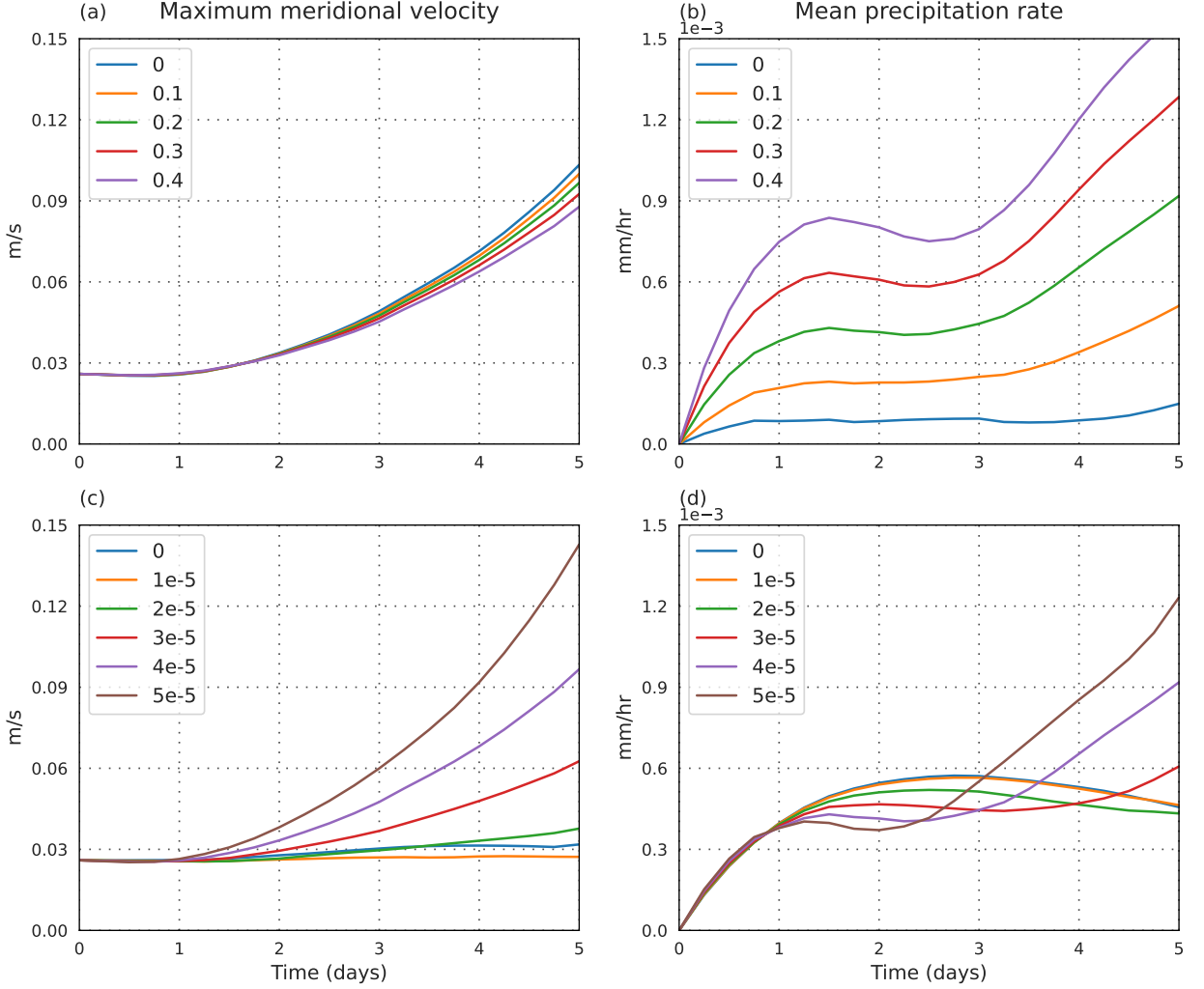


FIG. 8. Time series of the (a,c) maximum meridional velocity and (b,d) mean precipitation rate for the experiments with (a,b) varying basic-state moisture gradient (q_{sy}) and a horizontal wind shear of $\zeta_s = 4 \times 10^{-5} \text{ s}^{-1}$ and, (c,d) varying horizontal wind shear (ζ_s) with a basic-state moisture gradient of $q_{sy} = 0.2 \text{ m}$. These values are averaged over the entire domain and are the response to small amplitude sinusoidal vorticity anomalies.

where $h_{pert} = -15 \text{ m}$, λ is longitude, and the position and width parameters are $\lambda_0 = 180^\circ$, $\phi_0 = 20^\circ$, $\Delta\lambda = 5^\circ$, and $\Delta\phi = 5^\circ$. This yields an initial perturbation spanning a width of about 1000 km, with a balanced maximum meridional velocity of about 4.8 m s^{-1} , closely matching the peak rotational velocity in the initial anomaly imposed by Diaz and Boos (2021a).

The evolution of the initial vortex with a basic-state moisture gradient of $q_{sy} = 0.2 \text{ m}$ and a horizontal wind shear of $\zeta_s = 4 \times 10^{-5} \text{ s}^{-1}$ is shown in Figure 10. The initial vortex grows with

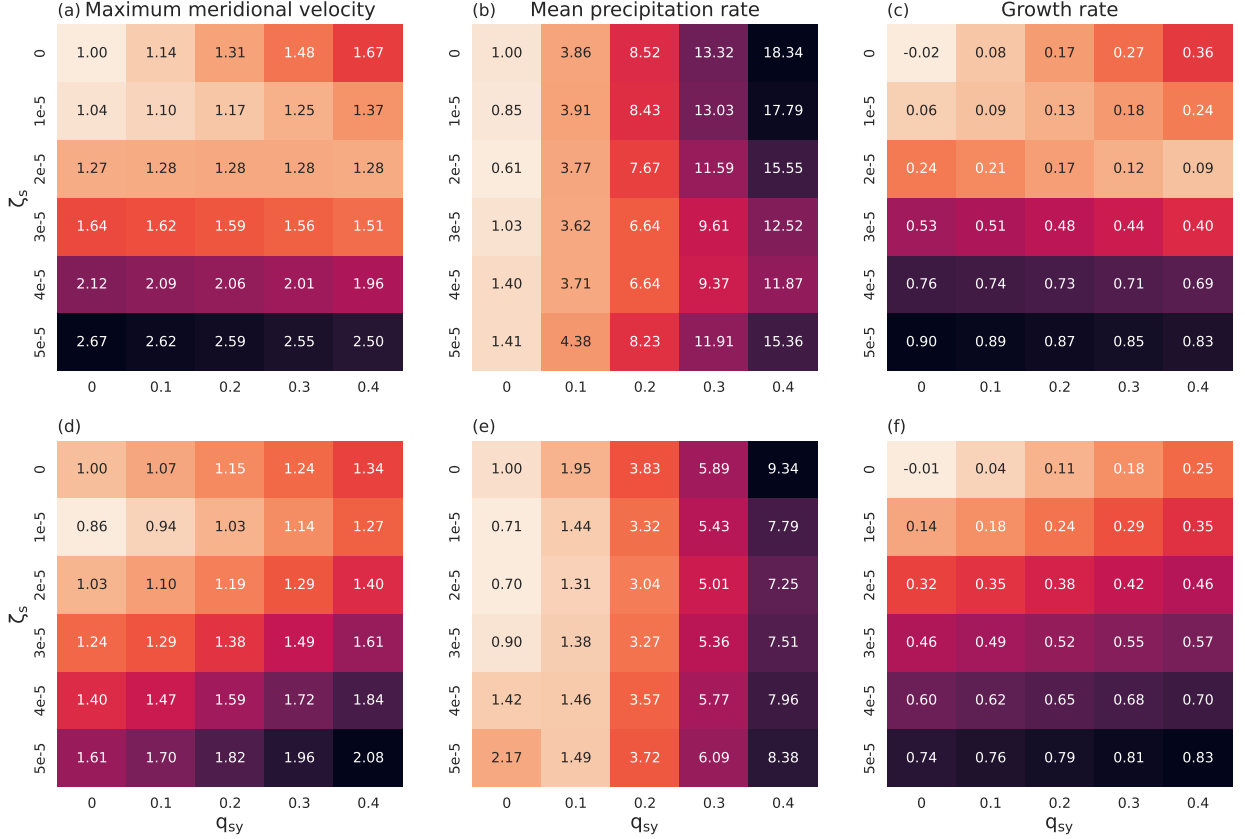


FIG. 9. Amplification of the (a,d) spatial maximum of meridional velocity and (b,e) spatial mean precipitation rate, and (c,f) eddy energy growth rate, all as a function of varying basic-state moisture gradient (q_{sy}) and horizontal wind shear (ζ_s). Panels in the first row (a–c) correspond to runs with weak sinusoidal modes and in second row (d–f) to runs with a finite-amplitude isolated vortex. The amplification of meridional velocity and precipitation rate is determined by taking the values at day 3 and normalizing by the corresponding values at day 3 for the moist run with no basic-state moisture gradient ($q_{sy} = 0$) and wind shear ($\zeta_s = 0$). Eddy energy includes both the eddy potential and kinetic energy, and the growth rates are averaged over days 2 to 4.

time, both spatially and in magnitude¹. For example, the maximum meridional velocity grows from its initial value of 4.8 m s^{-1} to about 8 m s^{-1} at the end of day 3. Similarly, precipitation intensifies and reaches its maximum around day 2. Although intense precipitation is also observed at later times, this occurs far east of the vortex centre associated with remote secondary disturbances

¹Although the increase in vortex size will contribute to the growth rate of eddy energy, the fact that the spatial maximum of meridional wind also increases strongly shows that the vortex intensity is also amplifying. Though we do not decompose the eddy energy growth rate into components associated with changes in vortex size and vortex intensity, we note that the fractional changes in meridional wind amplitude can account for a large part of the exponential growth rate in eddy energy. For example, comparing Figure 9d and Figure 9f, the peak eddy energy growth rate of 0.83 corresponds to an increase only slightly larger than the fractional increase of 2.08 seen in meridional wind ($e^{0.83} = 2.3$).

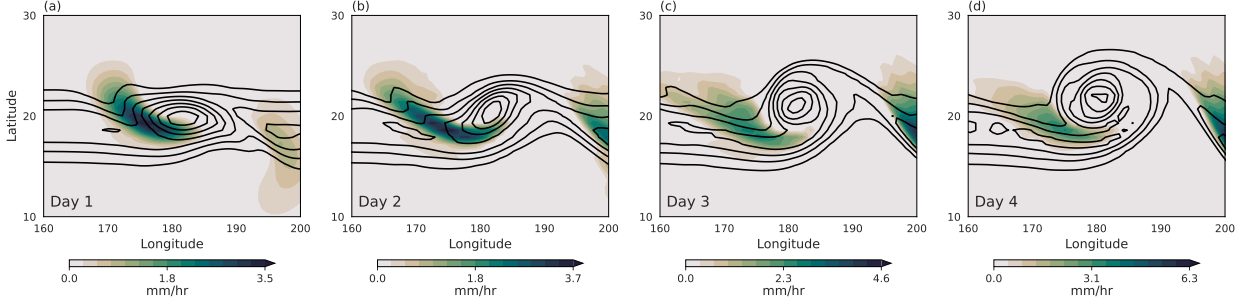


FIG. 10. The evolution of precipitation rate (color) and vorticity (black, with a contour interval of $1 \times 10^{-5} \text{ s}^{-1}$) with time for the experiment with a basic-state moisture gradient $q_{sy} = 0.2 \text{ m}$ and wind shear $\zeta_s = 4 \times 10^{-5} \text{ s}^{-1}$. A finite-amplitude isolated vortex is used to initialize the model.

(Figures 10c, d). Precipitation occurs to the west of the vortex centre because, in the presence of a poleward basic-state moisture gradient, northerly winds produce advective moistening west of the cyclonic vortex. This peak precipitation lies in roughly the same location that experiences quasigeostrophic (QG) lifting due to background vertical shear, which has been argued to produce precipitation in observed monsoon depressions (e.g. Rao and Rajamani 1970). But in our shallow water model that QG lifting does not operate because there is no background vertical shear.

We show the time evolution of the maximum meridional velocity and mean precipitation rate for varying moisture gradient with fixed horizontal shear (Figures 11a, b) and for a fixed moisture gradient with varying horizontal shear (Figures 11c, d). In these time series, we isolate the evolution of a single vortex by selecting a limited domain (a $20^\circ \times 20^\circ$ box) centred around the vorticity maximum, but we extend the zonal dimension by an additional 10° to the west for experiments with background moisture gradients and 10° to the east for experiments without those gradients. Although the size of this box exceeds the typical size of the observed LPS, we use this larger domain because the vortex in our idealized simulations grows beyond that typical size (Figure 10). This is a limitation of these idealized model configurations, which we speculate may permit such spatial growth because their background horizontal shear and moisture gradients extend over all longitudes. However, Diaz and Boos (2019a) showed that the mechanism of barotropic growth that operated in a zonally infinite region of background shear was still relevant when that shear zone was zonally confined.

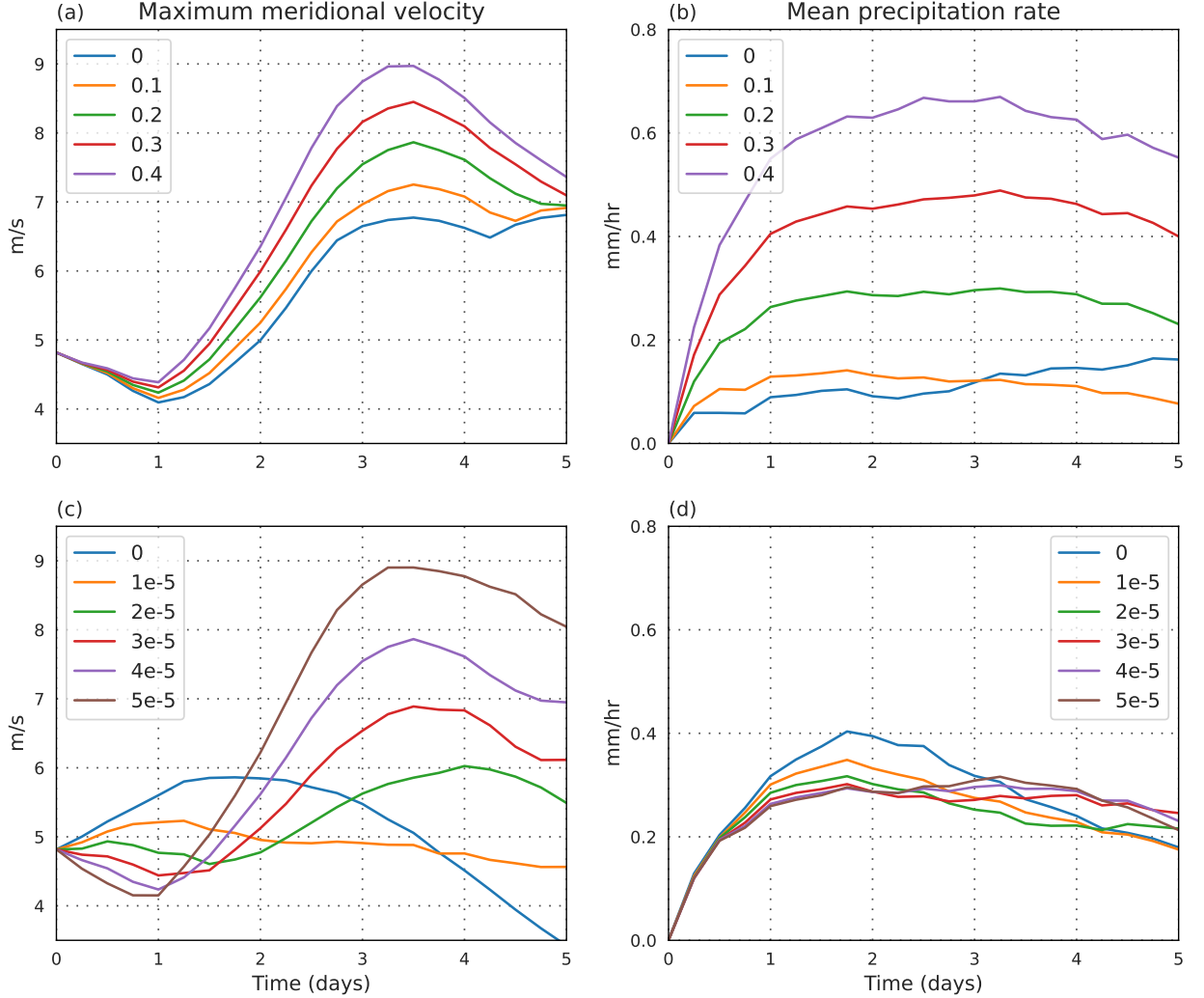


FIG. 11. Time series of the (a, c) maximum meridional velocity and (b, d) mean precipitation rate for the experiments with (a, b) varying basic-state moisture gradient (q_{sy}) and a horizontal wind shear of $\zeta_s = 4 \times 10^{-5} \text{ s}^{-1}$, and (c, d) varying horizontal wind shear (ζ_s) with a basic-state moisture gradient of $q_{sy} = 0.2 \text{ m}$. A finite-amplitude isolated vortex is used to initialize the model. We isolate the evolution of a single vortex by selecting a limited domain (a $20^\circ \times 20^\circ$ box) centred around the vorticity maximum, but we extend the zonal dimension by an additional 10° to the west for experiments with background moisture gradients and 10° to the east for experiments without those gradients.

When the basic-state moisture gradient (q_{sy}) is increased while keeping the horizontal shear (ζ_s) fixed, the amplification rates of meridional velocity and mean precipitation rate both increase, but the intensification of the precipitation rate is stronger than that of meridional winds (Figures 11a,

b). Conversely, when horizontal shear is increased for a fixed basic-state moisture gradient, the amplification rate of meridional wind increases while the precipitation rates change little (Figure 11c, d). In fact, the precipitation rate decreases by a small amount with increasing horizontal shear.

These results show that the isolated vortices exhibit similar sensitivities to basic-state properties as the small-amplitude sinusoidal modes. However, the sinusoidal modes continued to intensify past day 5, while the finite-amplitude vortex reaches its peak around day 3–4; while there are multiple possible causes of this, such as a resonance of the sinusoidal modes, the simplest explanation seems to be that nonlinearities associated with the stronger initial perturbation limit, or saturate, the growth². Furthermore, the growth of winds is more strongly affected by changes in the moisture gradient for the nonlinear, isolated vortex than for the quasi-linear sinusoidal modes. For example, the amplification of winds increases by a factor of about 1.5 when the basic-state moisture gradient is increased from $q_{sy} = 0$ to 0.2 m, similar to the idealized cloud-system-resolving simulations of Diaz and Boos (2021a); the shallow water model used here, however, permits testing of a wider range of q_{sy} . Nevertheless, when synthesizing results for all the experiments initialized with an isolated vortex, we see that the meridional velocity amplification and eddy growth rates are most sensitive to horizontal shear, while precipitation growth is set by the moisture gradient (Figures 9d-f), similar to the sensitivities of the quasi-linear sinusoidal modes (Figures 9a-c). Note that in these plots, as for the quasi-linear modes, the amplification of meridional velocity and precipitation rate are computed with respect to a moist run with no basic-state moisture gradient or horizontal shear ($q_{sy} = 0$ and $\zeta_s = 0$).

5. Phase relation between vorticity and precipitation

A pertinent question arises as to the mechanism of interaction between the two instability mechanisms. As discussed above, the growth of dynamic and convective fields seem to be somewhat decoupled, with the amplification of dynamical fields more strongly controlled by the horizontal shear, while precipitation growth is mostly determined by moisture gradients; this suggests interaction between the two instability mechanisms is weak. However, at stronger wind shears for the quasi-linear sinusoidal modes, the sensitivity of growth rates to the basic-state moisture gradient weakens and in some cases even hinders growth (Figures 9a, c). A possible

²The growth extends beyond 5 days for sinusoidal perturbations with other wavenumbers, although we do not provide illustrations of the simulation output for those runs. We also see the growth having a peak within the first 5 days when a stronger initial sinusoidal perturbation is used.

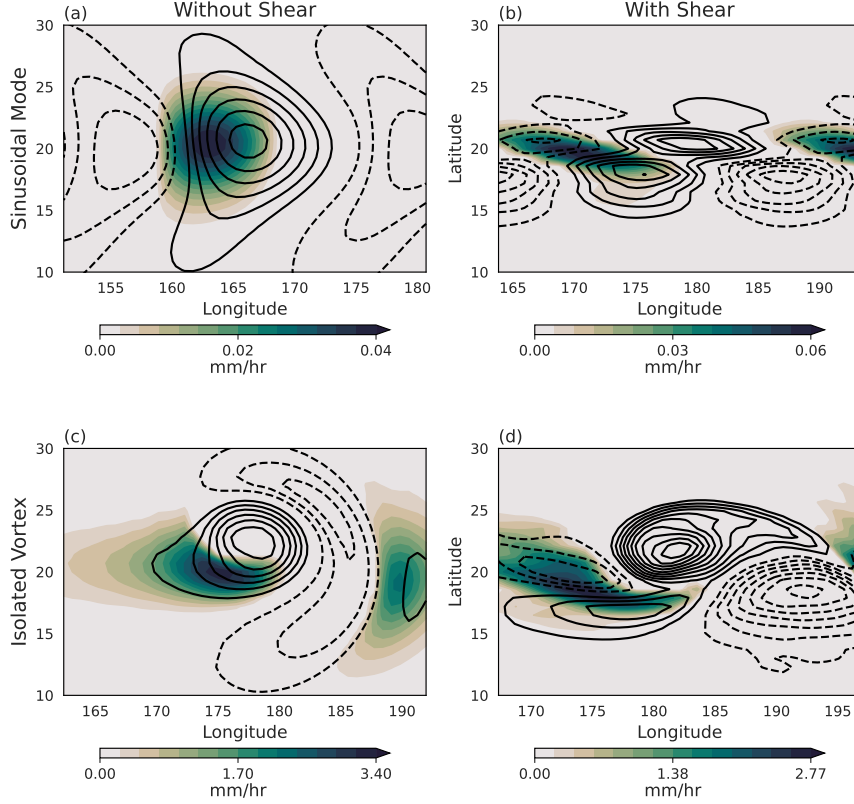


FIG. 12. Precipitation rate (color) and vorticity (black contours) at Day 3 for the experiments (a,c) without wind shear and (b,d) with a wind shear $\zeta_s = 4 \times 10^{-5} \text{ s}^{-1}$. All the plots have a basic-state moisture gradient of $q_{sy} = 0.2 \text{ m}$. Panels in the first row (a–b) correspond to runs with weak sinusoidal modes and in second row (c–d) to runs with a finite-amplitude isolated vortex. The basic-state vorticity strip is removed from the vorticity fields before plotting. The vorticity contour interval is (a) $2 \times 10^{-8} \text{ s}^{-1}$, (b) $5 \times 10^{-8} \text{ s}^{-1}$ and (c, d) $5 \times 10^{-6} \text{ s}^{-1}$.

explanation is that the phase relation between vorticity and precipitation which favors growth becomes distorted in the presence of strong horizontal shear. Figure 12 shows the anomalous vorticity and precipitation at day 3, for runs with a basic-state moisture gradient of $q_{sy} = 0.2 \text{ m}$ and both types of initial disturbance. Two cases are shown, one without horizontal shear and the other with shear of $\zeta_s = 4 \times 10^{-5} \text{ s}^{-1}$. In the absence of shear, precipitation peaks to the west of the cyclonic vortex centre (Figures 12a, c), which in linear theory is argued to favor intensification (Adames and Ming 2018a). However, with strong horizontal shear, this phase relation is distorted and precipitation aligns more closely with an anticyclonic centre (Figures 12b, d). This structure resembles the damped mode in the linear theory of Adames and Ming (2018a). This effect

seems to be stronger for the quasi-linear sinusoidal modes, but for nonlinear isolated vortices the sensitivities of the precipitation amplification rate and the eddy growth rate to the basic-state moisture gradient do decrease at higher horizontal shears (Figure 9e, f). The spatial structure of vorticity that is associated with this distortion of the moist effects by strong horizontal shear bears some resemblance to observations; the zonally elongated vorticity anomaly to the southwest of the main cyclonic vortex centre resembles that seen in a case study of a 2008 monsoon depression (Boos et al. 2017, their Figures 9, 10).

6. Summary and discussion

In this work, we aimed to understand the mechanism by which a monsoon depression-like vortex grows. With recent work noting the inconsistency of observed storm structures with the growth mechanism of baroclinic instability (Cohen and Boos 2016), we specifically examined the role played by two meridional gradients, in moisture and zonal wind shear, in their growth. Using a moist shallow water model in which we systematically varied these two gradients, we delineated the role played by moisture–vortex instability and barotropic growth in the intensification of initial disturbances.

To begin, we considered the growth of small-amplitude sinusoidal modes. In the absence of either a meridional moisture gradient or horizontal wind shear, that initial perturbation decayed with time, regardless of whether parameterized precipitation was included. This shows that at least one of the two gradients is essential for growth in our shallow water model. When only a moisture gradient was introduced, disturbance growth occurred in a phenomenon originally referred to as a balanced tropical moisture wave Sobel et al. (2001) and more recently termed moisture–vortex instability (Adames and Ming 2018a). With a poleward moisture gradient, the anomalies propagate westward with precipitation occurring to the west of the vorticity maxima. This leads to an enhancement of the vortex, with larger growth rates occurring as the basic-state moisture gradient was increased. The precipitation rates exhibited greater sensitivity than the vortex strength to changes in the moisture gradient. Overall, our low-amplitude (and thus quasi-linear) solutions in a spherical domain resembled the linear solutions obtained by Adames and Ming (2018a), with similar sensitivity to several model parameters. When meridional wind shear was instead imposed in the basic-state, the intensification rate of horizontal winds increased with

443 the shear but precipitation rates were weaker than in the presence of a moisture gradient and were
444 comparatively insensitive to the shear. Also, in contrast to observations, precipitation occurred to
445 the east of the vortex centres. In the presence of both a moisture gradient and wind shear in the
446 basic-state, the growth of dynamical fields was mainly controlled by the shear, while precipitation
447 rates were mostly set by the moisture gradient.

448 A broadly similar picture emerged from our examination of the evolution of a finite-amplitude
449 isolated vortex, with the growth of the dynamical fields being more sensitive to the horizontal shear
450 than to the moisture gradient. However, the moisture gradient did affect the growth of dynamical
451 fields to a greater extent than for the small-amplitude sinusoidal initial condition. Similar to
452 the cloud-resolving simulation of Diaz and Boos (2021a), we saw an amplification of the winds
453 by a factor of about 1.5 because of the inclusion of a moisture gradient in the basic-state. The
454 precipitation rate for the isolated vortex was mostly set by the moisture gradient, as in the quasi-
455 linear sinusoidal modes. However, in contrast to those quasi-linear modes where the intensification
456 occurred even after day 5, the vortex strength and precipitation rate peaked around day 3–4,
457 suggesting the importance of non-linear effects.

458 Acting alone, both barotropic and moisture–vortex instabilities lead to an intensification of an
459 isolated vortex or a quasi-linear sinusoidal mode. But in combination their effects weaken slightly,
460 as evidenced by a smaller sensitivity of growth rates to the basic-state gradients. Especially
461 for strong wind shear, the contribution of moisture–vortex instability diminishes and in some
462 case even hinders disturbance growth. A possible explanation lies in the distortion of the phase
463 relation between moisture anomalies and vorticity anomalies with increasing shear, which seems
464 to disrupt the moisture–vortex instability. It is possible that interaction of the barotropic and
465 moisture-vortex instabilities would change with different magnitudes and spatial structures of the
466 background gradients. For example, for stronger background wind shears, the vortex amplification
467 may be almost entirely due to barotropic growth if the background shears sufficiently distort the
468 vortex’s phase relation with moisture anomalies. The interaction of the two instabilities may also
469 be influenced by the meridional width and zonal extent of the background gradients; indeed, the
470 meridional shear associated with the observed monsoon trough over South Asia typically has a
471 different meridional position and meridional width than the background moisture gradient (e.g.
472 Figure 1), as well as a somewhat different zonal extent. However, even in the absence of a true

instability, moisture gradients may still alter precipitation by producing moisture advection or modifying the moisture content in regions experiencing dynamical lifting.

Even in the absence of any disruption of one instability mechanism by another, our results highlight the possibility that rotational winds in a lower-tropospheric vortex can intensify at different rates than the precipitating ascent in such a vortex. In other words, LPS need not have vertical and horizontal motion fields with fixed relative amplitudes; barotropic instability is a canonical example of a mechanism that primarily intensifies the rotational flow, and Diaz and Boos (2019b) argued that vertical motions might be generated in the presence of such barotropic growth primarily through dynamical coupling with a background vertical shear (e.g. via QG lifting). Our shallow water model does not include any representation of such vertical shear, so it is a framework in which the barotropic growth mechanism can be cleanly isolated from other diabatic mechanisms (such as moisture-vortex instability).

The presence of vertical shear and associated QG lifting has long been thought to influence precipitation in monsoon depressions (Rao and Rajamani 1970; Sanders 1984), with the location of peak precipitation well predicted by solutions of the adiabatic QG omega equation (Boos et al. 2015). The dynamical lifting produced by the interaction of the vortex with the background vertical shear been argued to be amplified by a feedback with moist convection, thereby enhancing monsoon depression precipitation (Nie and Sobel 2016; Murthy and Boos 2020). However, in our single-layer shallow water model, vertical shear is not included and the effect of QG lifting is ignored, which is a limitation of this study. It is unclear whether this is a major deficiency, because in the idealized cloud-system-resolving simulations of Diaz and Boos (2021a), vertical shear was found to be important in monsoon depression amplification primarily through its effect on the meridional moisture gradient (their basic-state used constant relative humidity, so any vertical shear was accompanied by a moisture gradient, through thermal wind balance). That effect is represented in our shallow water model by the prescription of an initial moisture gradient and a saturation moisture gradient. Whether QG lifting due to vertical shear is additionally important for amplification merits further exploration.

The result that both meridional moisture gradients and meridional wind shear may be vital for the growth of monsoon depressions was suggested by Diaz and Boos (2021a), but the convection-permitting simulations used in that study did not allow the wide exploration of parameter space

undertaken here. Furthermore, the existence of differing sensitivities of the vortex intensification rate and the precipitation intensification rate to these two environmental gradients is a novel finding. Further work needs to be done to determine whether these results are affected by QG uplift due to coupling with background vertical shear, stratification, or other effects that cannot be represented in a two-dimensional shallow water model.

In addition to further modeling for the goal of understanding mechanisms, a useful next step might be to examine the consistency of the mechanisms described here with the observed amplification of monsoon depressions. Other future work might explore the implications of these results for forecasts of monsoon LPS. For example, the dry bias in low-level relative humidity seen in a high-resolution numerical model used for weather forecasting over India (Mukhopadhyay et al. 2019) may explain why that model has biases in its representation of the intensification of monsoon LPS (Sarkar et al. 2021). These issues have great importance for disaster preparedness, given the large fraction of South Asian hydrological disasters that are associated with monsoon LPS (Suhas et al. 2022).

Acknowledgments. The authors acknowledge financial support from the Earth System Science Organization, Ministry of Earth Sciences, Government of India (Grant IITM/MM-II/Univ_California_USA/INT-3) to conduct this research under the Monsoon Mission. The authors also acknowledge support from the U.S. Department of Energy, Office of Science, Office of Biological and Environmental Research, Climate and Environmental Sciences Division, Regional and Global Model Analysis Program, under Award DE-SC0019367. This work used resources of the National Energy Research Scientific Computing Center (NERSC), which is a DOE Office of Science User Facility.

Data availability statement. The moist shallow water code used to run the simulations is available on GitHub (<https://github.com/suhasdl/pySWE>). ERA5 data was downloaded from the Copernicus Climate Change Service Climate Data Store (CDS) website (<https://cds.climate.copernicus.eu>). Numerical simulation data are available from the authors upon request.

References

Adames, Á. F. (2021). Interactions between water vapor, potential vorticity, and vertical wind shear in quasi-geostrophic motions: Implications for rotational tropical motion systems. *Journal of the Atmospheric Sciences*, 78(3):903–923.

- 532 Adames, Á. F. and Ming, Y. (2018a). Interactions between water vapor and potential vorticity in
533 synoptic-scale monsoonal disturbances: Moisture vortex instability. *Journal of the Atmospheric*
534 *Sciences*, 75(6):2083–2106.
- 535 Adames, Á. F. and Ming, Y. (2018b). Moisture and moist static energy budgets of south asian
536 monsoon low pressure systems in gfdl am4. 0. *Journal of the Atmospheric Sciences*, 75(6):2107–
537 2123.
- 538 Ajayamohan, R., Merryfield, W. J., and Kharin, V. V. (2010). Increasing trend of synoptic activity
539 and its relationship with extreme rain events over central india. *Journal of Climate*, 23(4):1004–
540 1013.
- 541 Bembenek, E., Merlis, T. M., and Straub, D. N. (2021). Influence of latitude and moisture
542 effects on the barotropic instability of an idealized itcz. *Journal of the Atmospheric Sciences*,
543 78(9):2677–2689.
- 544 Betts, A. K. (1986). A new convective adjustment scheme. part i: Observational and theoretical
545 basis. *Quarterly Journal of the Royal Meteorological Society*, 112(473):677–691.
- 546 Boos, W., Hurley, J., and Murthy, V. (2015). Adiabatic westward drift of indian monsoon depres-
547 sions. *Quarterly Journal of the Royal Meteorological Society*, 141(689):1035–1048.
- 548 Boos, W. R., Mapes, B. E., and Murthy, V. S. (2017). Potential vorticity structure and propagation
549 mechanism of indian monsoon depressions. In *The Global Monsoon System: Research and*
550 *Forecast*, pages 187–199. World Scientific.
- 551 Bouchut, F., Lambaerts, J., Lapeyre, G., and Zeitlin, V. (2009). Fronts and nonlinear waves in
552 a simplified shallow-water model of the atmosphere with moisture and convection. *Physics of*
553 *Fluids*, 21(11):116604.
- 554 Chen, X., Pauluis, O. M., Leung, L. R., and Zhang, F. (2018). Multiscale atmospheric overturning
555 of the indian summer monsoon as seen through isentropic analysis. *Journal of the Atmospheric*
556 *Sciences*, 75(9):3011–3030.
- 557 Clark, S. K., Ming, Y., and Adames, Á. F. (2020). Monsoon low pressure system–like variability
558 in an idealized moist model. *Journal of Climate*, 33(6):2051–2074.

559 Cohen, N. Y. and Boos, W. R. (2016). Perspectives on moist baroclinic instability: Implications
560 for the growth of monsoon depressions. *Journal of the Atmospheric Sciences*, 73(4):1767–1788.

561 Diaz, M. and Boos, W. R. (2019a). Barotropic growth of monsoon depressions. *Quarterly Journal*
562 *of the Royal Meteorological Society*, 145(719):824–844.

563 Diaz, M. and Boos, W. R. (2019b). Monsoon depression amplification by moist barotropic
564 instability in a vertically sheared environment. *Quarterly Journal of the Royal Meteorological*
565 *Society*, 145(723):2666–2684.

566 Diaz, M. and Boos, W. R. (2021a). Evolution of idealized vortices in monsoon-like shears:
567 Application to monsoon depressions. *Journal of the Atmospheric Sciences*, 78(4):1207–1225.

568 Diaz, M. and Boos, W. R. (2021b). The influence of surface heat fluxes on the growth of idealized
569 monsoon depressions. *Journal of the Atmospheric Sciences*, 78(6):2013–2027.

570 Fletcher, J. K., Parker, D. J., Hunt, K. M., Vishwanathan, G., and Govindankutty, M. (2018). The
571 interaction of indian monsoon depressions with northwesterly midlevel dry intrusions. *Monthly*
572 *Weather Review*, 146(3):679–693.

573 Frierson, D. M., Majda, A. J., and Pauluis, O. M. (2004). Large scale dynamics of precipitation
574 fronts in the tropical atmosphere: A novel relaxation limit. *Communications in Mathematical*
575 *Sciences*, 2(4):591–626.

576 Galewsky, J., Scott, R. K., and Polvani, L. M. (2004). An initial-value problem for testing
577 numerical models of the global shallow-water equations. *Tellus A: Dynamic Meteorology and*
578 *Oceanography*, 56(5):429–440.

579 Gill, A. E. (1982). Studies of moisture effects in simple atmospheric models: The stable case.
580 *Geophysical & Astrophysical Fluid Dynamics*, 19(1-2):119–152.

581 Godbole, R. V. (1977). The composite structure of the monsoon depression. *Tellus*, 29(1):25–40.

582 Goswami, B. N., Keshavamurty, R., and Satyan, V. (1980). Role of barotropic, baroclinic and
583 combined barotropic-baroclinic instability for the growth of monsoon depressions and mid-
584 tropospheric cyclones. *Proceedings of the Indian Academy of Sciences-Earth and Planetary*
585 *Sciences*, 89(1):79–97.

586 Hunt, K. M. and Fletcher, J. K. (2019). The relationship between indian monsoon rainfall and
587 low-pressure systems. *Climate Dynamics*, 53(3):1859–1871.

588 Hurley, J. V. and Boos, W. R. (2015). A global climatology of monsoon low-pressure systems.
589 *Quarterly Journal of the Royal Meteorological Society*, 141(689):1049–1064.

590 Keshavamurty, R. (1972). On the vertical tilt of monsoon disturbancy. *Journal of Atmospheric*
591 *Sciences*, 29(5):993–994.

592 Kiladis, G. N., Wheeler, M. C., Haertel, P. T., Straub, K. H., and Roundy, P. E. (2009). Convectively
593 coupled equatorial waves. *Reviews of Geophysics*, 47(2).

594 Kraucunas, I. and Hartmann, D. L. (2007). Tropical stationary waves in a nonlinear shallow-water
595 model with realistic basic states. *Journal of the atmospheric sciences*, 64(7):2540–2557.

596 Krishnakumar, V., Keshavamurty, R., and Kasture, S. (1992). Moist baroclinic instability and
597 the growth of monsoon depressions—linear and nonlinear studies. *Proceedings of the Indian*
598 *Academy of Sciences-Earth and Planetary Sciences*, 101(2):123–152.

599 Krishnamurti, T., Martin, A., Krishnamurti, R., Simon, A., Thomas, A., and Kumar, V. (2013).
600 Impacts of enhanced ccn on the organization of convection and recent reduced counts of monsoon
601 depressions. *Climate dynamics*, 41(1):117–134.

602 Krishnamurti, T. N., Kanamitsu, M., Godbole, R., Chang, C.-B., Carr, F., and Chow, J. H. (1976).
603 Study of a monsoon depression (ii), dynamical structure. *Journal of the Meteorological Society*
604 *of Japan. Ser. II*, 54(4):208–225.

605 Lambaerts, J., Lapeyre, G., and Zeitlin, V. (2011). Moist versus dry barotropic instability in a
606 shallow-water model of the atmosphere with moist convection. *Journal of the Atmospheric*
607 *Sciences*, 68(6):1234–1252.

608 Lambaerts, J., Lapeyre, G., and Zeitlin, V. (2012). Moist versus dry baroclinic instability in a
609 simplified two-layer atmospheric model with condensation and latent heat release. *Journal of*
610 *the Atmospheric Sciences*, 69(4):1405–1426.

611 Lindzen, R., Farrell, B., and Rosenthal, A. (1983). Absolute barotropic instability and monsoon
612 depressions. *Journal of Atmospheric Sciences*, 40(5):1178–1184.

613 Mishra, S. and Salvekar, P. (1980). Role of baroclinic instability in the development of monsoon
614 disturbances. *Journal of Atmospheric Sciences*, 37(2):383–394.

615 Monteiro, J. M., Adames, Á. F., Wallace, J. M., and Sukhatme, J. S. (2014). Interpreting the upper
616 level structure of the madden-julian oscillation. *Geophysical Research Letters*, 41(24):9158–
617 9165.

618 Moorthi, S. and Arakawa, A. (1985). Baroclinic instability with cumulus heating. *Journal of*
619 *Atmospheric Sciences*, 42(19):2007–2031.

620 Mukhopadhyay, P., Prasad, V., Krishna, R., Deshpande, M., Ganai, M., Tirkey, S., Sarkar, S.,
621 Goswami, T., Johny, C., Roy, K., et al. (2019). Performance of a very high-resolution global
622 forecast system model (gfs t1534) at 12.5 km over the indian region during the 2016–2017
623 monsoon seasons. *Journal of Earth System Science*, 128(6):1–18.

624 Muller, C. J., Back, L. E., O’Gorman, P. A., and Emanuel, K. A. (2009). A model for the relationship
625 between tropical precipitation and column water vapor. *Geophysical Research Letters*, 36(16).

626 Murthy, V. S. and Boos, W. R. (2018). Role of surface enthalpy fluxes in idealized simulations of
627 tropical depression spinup. *Journal of the Atmospheric Sciences*, 75(6):1811–1831.

628 Murthy, V. S. and Boos, W. R. (2020). Quasigeostrophic controls on precipitating ascent in
629 monsoon depressions. *Journal of the Atmospheric Sciences*, 77(4):1213–1232.

630 Nie, J. and Sobel, A. H. (2016). Modeling the interaction between quasigeostrophic vertical motion
631 and convection in a single column. *Journal of the Atmospheric Sciences*, 73(3):1101–1117.

632 Nitta, T. and Masuda, K. (1981). Observational study of a monsoon depression developed over the
633 bay of bengal during summer monex. *Journal of the Meteorological Society of Japan. Ser. II*,
634 59(5):672–682.

635 Paldor, N., Shamir, O., and Garfinkel, C. I. (2021). Barotropic instability of a zonal jet on the sphere:
636 from non-divergence through quasi-geostrophy to shallow water. *Geophysical & Astrophysical*
637 *Fluid Dynamics*, 115(1):15–34.

638 Peng, J., Li, T., Peng, M. S., and Ge, X. (2009). Barotropic instability in the tropical cyclone outer
639 region. *Quarterly Journal of the Royal Meteorological Society: A journal of the atmospheric*
640 *sciences, applied meteorology and physical oceanography*, 135(641):851–864.

641 Rajamani, S. and Sikdar, D. (1989). Some dynamical characteristics and thermal structure of
642 monsoon depressions over the bay of bengal. *Tellus A*, 41(3):255–269.

643 Rao, K. and Rajamani, S. (1970). Diagnostic study of a monsoon depression by geostrophic
644 baroclinic model. *MAUSAM*, 21(2):187–194.

645 Rostami, M. and Zeitlin, V. (2017). Influence of condensation and latent heat release upon
646 barotropic and baroclinic instabilities of vortices in a rotating shallow water f-plane model.
647 *Geophysical & Astrophysical Fluid Dynamics*, 111(1):1–31.

648 Rostami, M. and Zeitlin, V. (2019a). Eastward-moving convection-enhanced modons in shallow
649 water in the equatorial tangent plane. *Physics of Fluids*, 31(2):021701.

650 Rostami, M. and Zeitlin, V. (2019b). Geostrophic adjustment on the equatorial beta-plane revisited.
651 *Physics of Fluids*, 31(8):081702.

652 Rydbeck, A. V. and Maloney, E. D. (2014). Energetics of east pacific easterly waves during
653 intraseasonal events. *Journal of Climate*, 27(20):7603–7621.

654 Saha, K. and Chang, C. (1983). The baroclinic processes of monsoon depressions. *Monthly*
655 *weather review*, 111(7):1506–1514.

656 Salvekar, P., George, L., and Mishra, S. (1986). Low level wind shear and baroclinic growth of
657 monsoon depression scale waves. *Meteorology and Atmospheric Physics*, 35(1):10–18.

658 Sanders, F. (1984). Quasi-geostrophic diagnosis of the monsoon depression of 5–8 july 1979.
659 *Journal of Atmospheric Sciences*, 41(4):538–552.

660 Sarkar, S., Mukhopadhyay, P., Dutta, S., Phani Murali Krishna, R., Kanase, R. D., Prasad, V., and
661 Deshpande, M. S. (2021). Gfs model fidelity in capturing the transition of low-pressure area to
662 monsoon depression. *Quarterly Journal of the Royal Meteorological Society*, 147(738):2625–
663 2637.

664 Schaeffer, N. (2013). Efficient spherical harmonic transforms aimed at pseudospectral numerical
665 simulations. *Geochemistry, Geophysics, Geosystems*, 14(3):751–758.

666 Shukla, J. (1977). Barotropic-baroclinic instability of mean zonal wind during summer monsoon.
667 *Pure and applied geophysics*, 115(5):1449–1461.

668 Sikka, D. (1978). Some aspects of the life history, structure and movement of monsoon depressions.
669 In *Monsoon dynamics*, pages 1501–1529. Springer.

670 Sobel, A. H., Nilsson, J., and Polvani, L. M. (2001). The weak temperature gradient approximation
671 and balanced tropical moisture waves. *Journal of the atmospheric sciences*, 58(23):3650–3665.

672 Subrahmanyam, D., Tandon, M., George, L., and Mishra, S. (1981). Role of barotropic mechanism
673 in the development of a monsoon depression: A monex study. *pure and applied geophysics*,
674 119(5):901–912.

675 Suhas, D. L., Ramesh, N., Kripa, R. M., and Boos, W. R. (2022). Influence of monsoon low
676 pressure systems on south asian disasters and implications for disaster prediction.

677 Suhas, D. L. and Sukhatme, J. (2020). Moist shallow-water response to tropical forcing: Initial-
678 value problems. *Quarterly Journal of the Royal Meteorological Society*, 146(733):3695–3714.

679 Wheeler, M., Kiladis, G. N., and Webster, P. J. (2000). Large-scale dynamical fields associated with
680 convectively coupled equatorial waves. *Journal of the Atmospheric Sciences*, 57(5):613–640.

681 Zeitlin, V. (2018). *Geophysical fluid dynamics: understanding (almost) everything with rotating*
682 *shallow water models*. Oxford University Press.